Title

Size-Dependent Chemomechanical Failure of Sulfide Solid Electrolyte Particles during Electrochemical Reaction with Lithium

Journal

Nano Letters, 22(1)

ISSN

1530-6984

Authors

Zhao, Jun

Zhao, Chao

Zhu, Jianping

et al.

Publication Date

2022-01-12

DOI

10.1021/acs.nanolett.1c04076

Size dependent chemomechanical failure of sulfide solid electrolyte particles during electrochemical reaction with lithium

Jun Zhao[1,#], Chao Zhao[2,#], Jianping Zhu[3], Xiangsi Liu[3], Jingming Yao[1], Bo Wang[1], Qiushi Dai[1], Zaifa Wang[1], Jingzhao Chen[1], Peng Jia[1], Yanshuai Li[1], Stephen J. Harris[4], Yong Yang[3], Yongfu Tang [1,5,], Liqiang Zhang[1,*], Feng Ding[2,*], Jianyu Huang[1,6,*]*

[1]Clean Nano Energy Center, State Key Laboratory of Metastable Materials Science and Technology, Yanshan University, Qinhuangdao 066004, P. R. China.

[2]Institute for Basic Science (IBS), School of Materials Science and Engineering, Ulsan National Institute of Science and Technology (UNIST), Ulsan 44919, Republic of Korea.

[3]Collaborative Innovation Center of Chemistry for Energy Materials, State Key Laboratory for Physical Chemistry of Solid Surface, College of Chemistry and Chemical Engineering, Xiamen University, Xiamen 361005, P. R. China.

[4]Energy Storage Division, Lawrence Berkeley, National Laboratory, Berkeley, CA 94720, USA.

[5]Hebei Key Laboratory of Applied Chemistry, College of Environmental and Chemical Engineering, Yanshan University, Qinhuangdao 066004, P. R. China.

[6]School of Materials Science and Engineering, Xiangtan University, Xiangtan, Hunan 411105, P. R. China.

[#]These authors contributed equally.

Corresponding Author

*Correspondence to: jyhuang8@hotmail.com; f.ding@unist.ac.kr; lqzhang@ysu.edu.cn; tangyongfu@ysu.edu.cn.

KEYWORDS: *Solid-state batteries, Chemomechanical failure, Size effect, Sulfide solid electrolyte*

ABSTRACT: The very high ionic conductivity of $Li_{10}GeP_2S_{12}$ (LGPS) solid electrolyte (SE) makes it a promising candidate SE for solid-state batteries in electrical vehicles. However, chemomechanical failure, whose mechanism remains unclear, has plagued its widespread applications. Herein we report in situ imaging lithiation induced failure of LGPS SE. We revealed a strong size effect in the chemomechanical failure of LGPS particles: namely, when the particle size is greater than 3 μm, fracture/pulverization occurred; when the particle size is between 1 μm and 3 μm, microcracks emerged; when the particle size is less than 1 μm, no chemomechanical failure was observed. This strong size effect is interpreted by the interplay between elastic energy storage and dissipation. Our finding has important implications for the design of high-performance LGPS SE, for example, by reducing the particle size to less than 1 μm, the chemomechanical failure of LGPS SE can be mitigated.

■ INTRODUCTION

Solid-state batteries (SSBs) are potential next-generation energy storage technology to replace existing liquid electrolyte batteries. The critical component of a SSB is the solid electrolyte (SE). $Li_{10}GeP_2S_{12}$ (LGPS) SE has an extremely high ionic conductivity of 12 mS cm^{-1} which is even higher than those of organic liquid electrolytes currently used in practical lithium-ion batteries[1]. The very high ionic conductivity makes LGPS a promising candidate SE for SSBs in electrical vehicles and grid storage systems. However, besides the high ionic conductivity of SE, good electro-chemo-mechanical stability with electrodes, particularly in contact with the lithium anode, are also strongly required. Unfortunately, LGPS is thermodynamically unstable with lithium[2, 3]. It reacts with lithium to form Li_2S, Li_3P and $Li_{3.75}Ge_4$[4-8], causing large volume expansion of the interphase, thus stresses and cracks inside the SEs[9-12]. Once crack forms, lithium penetration and short circuit are inevitable[13-25]. Understanding the electro-chemo-mechanical failure mechanism is thus critical for the application of LGPS in SSBs. Nevertheless, due to the extreme sensitivity of LGPS to air exposure and humidity[26], in situ electron microscopy observation of the interface between LGPS and lithium metal during the electrochemical process has not been achieved due to the technical difficulty in sample preparation, transfer and manipulation.

Herein, we succeed in constructing a home-made two-terminal electrochemical device in a dual beam focused ion beam (FIB) electron microscope, enabling real-time observations of the electrochemical reaction between lithium and LGPS. Surprisingly, we find a strong size-dependent electro-chemo-mechanical fracture behavior of individual LGPS particles, namely, fracture and pulverization of LGPS particles occur when the particle size is above 3 μm; no fracture of the LGPS particles takes place when the particle size is less than 1 μm; microcracks but not pulverization are observed when the particle size is between 1 and 3 μm. A theoretical model together with finite element simulation revealed that the electro-chemo-mechanical strain energy is not high enough to drive crack nucleation and propagation in LGPS particles when their sizes are less than 1 μm. Our discovery provides important insight towards mitigating the failure of LGPS SEs, i.e., by controlling the particle size of LGPS SE to less than 1 μm, fracture of the LGPS SE can be alleviated.

■ RESULTS AND DISCUSSION

A schematic of our experimental setup is shown in Figure 1a. The W tip (tungsten tip) of the manipulator was used as a working electrode, and the FIB stage where Li metal was attached was used as the counter electrode. Lithium metal and LGPS were assembled on the FIB sample stub in a glove box and then transferred to the FIB using a home-made vacuum transfer box. For a better contact between the W tip and the SE, indium metal was attached to the W tip. A LGPS particle with a size of 30 μm was compressed by the W tip. During compression, the LGPS particle was pushed into the lithium substrate, rendering a good contact between lithium and the LGPS particle (Figure 1b); in the meantime, a good contact between LGPS and indium was also established during the compression (Figure 1b). Note that the structure of the LGPS particle remains perfect after compression, with no crack on its surface, indicating that compression did not fracture the LGPS particle (Figure 1b). Upon applying a negative potential on the indium electrode, lithiation of indium took place, as revealed by the contrast change in the indium metal (Figure 1b, c). The lithiation proceeded extremely fast from the contact between LGPS and indium, then advanced upward the indium electrode (Figure 1b, c), and the lithiation of the indium electrode was completed within a few seconds. After full lithiation of indium, microcracks emerged in the LGPS particle (arrowheads, Figure 1c). With the passage of time, the number and sizes of the cracks increased (Figure 1c-f, Supplementary Movie S1), until the whole particle was pulverized (Figure 1f). Two more examples are exemplified in Figure S1 and Supplementary Movie S2, which shows that the crack was generated at the W tip contact and gradually extended downward until the whole particle was pulverized. It is interesting to note that when we used W tip instead of indium electrode, some Li would be first deposited on the W tip, followed by the appearance of SE cracking and gradually pulverization (Supplementary Movie S2). To avoid the influence of the W tip pressure on the mechanical behavior of the SE, we conducted another similar lithiation experiment via connecting the W tip to the side of the LGPS particle, in which no significant stress was exerted to the SE particles by the W tip. Nevertheless, similar chemomechanical failure mechanism was also observed (Figure S2).

Figure 1g-j displays the pulverization of another LGPS particle with a size of 30 μm. After 689 s of lithiation, the initial perfect LGPS particle (Figure 1g) pulverized (Figure 1h). Figure 1i, j are magnified images of the areas outlined in two boxes marked as "i" and "j" in Figure 1h,

respectively, showing the interfaces between the reacted (darker contrast) and unreacted (brighter contrast) portions of the same particle. It can be seen that as soon as the reaction front extended, cracks emerged right behind the reaction front (yellow dashed lines). However, the pulverization exhibited hysteresis compared to the reaction process (green dashed lines in Figure 1i), suggesting a progressive lithiation of the LGPS particle, and the crack and pulverization were caused by lithiation. Unlike traditional in situ transmission electron microscopy (TEM) studies of nano-batteries[27-29], here, the lithiation process of LGPS SE started from the end far away from the negative Li electrode. It is traditionally believed that a violent electrochemical reaction would take place at the interface between the active SE and Li negative electrode. However, we found in this study that the highly-reactive fresh Li deposited on the W tip is more likely to react with the SE. As shown in Figure S3 and Supplementary Movie S3, Li ions initially passed through the SE and deposited as lithium dendrtie underneath the W tip. Electrochemical reaction quickly happened between the freshly deposited Li and the SE until the full pulverization of the SE. Ye et al. reported that the LGPS SEs, which is electrochemically unstable against Li metal, can be used as an intermediate electrolyte layer and consume some lithium dendrites[12]. However, the cycling performance of LGPS based batteries would be greatly compromised if the pulverization process continuously happens. Moreover, the newly generated cracks also provide a fast channel for lithium dendrite penetration. As shown in Figure S4 and Supplementary Movie S4, lithium dendrite penetration becomes inevitable once cracks are formed. Lithium dendrites emerged from the cracks and lead to further growth of cracks. Fortunately, through a large number of experiments, we find that reducing the particle size of LGPS can effectively avoid the pulverization and crack generation of the LGPS SE.

Figure 2 demonstrates the strong size effect of the fracture and pulverization of LGPS particles. When the particle size is larger than 3 μm, e.g., Figure 2a, cracks formed (Figure 2b) and proliferated (Figure 2b-d) until pulverization (Figure 2d, Supplementary Movie S5) of the entire particle. When the size is between 1 and 3 μm, e.g., Figure 2e, cracks formed but no pulverization took place in the particle (Figure 2f-h, Figure S5, Supplementary Movie S6). When the particle is less than 1 μm, cracks barely formed in the nanoparticle (Figure 2i-l, Figure S6, Supplementary Movie S7). We conducted a series of statistical experiments, which confirms the above assessment (Figure 2m). Meanwhile, we conducted additional experiments to investigate the pulverization of the particles in a SE pellet that was prepared under high pressure. Size dependent

chemomechanical failure was also observed from the above LGPS pellet, which is consistent with the single particle result (Figure S7 and Figure S8).

To understand the electro-chemo-mechanics of the size effect, we performed in situ TEM study of the lithium reaction with LGPS particles. The initial LGPS has a tetragonal structure ($P4_2/nmc$) with $a = b = 8.71$ Å and $c = 12.61$ Å (Figure 3a, b). Selected area electron diffraction pattern (SAED) indicates that each individual particle is a single crystal (Figure 3c, d). The in situ TEM procedure is schematically illustrated in Figure 3e and Supplementary methods. Pieces of lithium metal were scratched into a Cu grid, then LGPS particles were drop cast onto the TEM grid. Some of the LGPS particles ended up landing on the lithium metal. We then placed the electron beam near the LGPS particle (but not on the particle as LGPS is sensitive to the electron beam), and lithium diffused to the LGPS particle under the electron irradiation. Consequently, chemical reactions between lithium and LGPS particles occurred (Figure 3f-k). The pristine LGPS nanoparticle with a size of 700 nm (Figure 3f) swelled to 800 nm after lithiation (Figure 3g) with a volume expansion of about 14%. SAED indicates that the initial single crystal (Figure 3h) transformed into nanocrystalline Li_2S (Figure 3i). The changes in the electronic structure were investigated by electron energy loss spectroscopy (EELS). Low-loss EELS of the pristine LGPS exhibits a major plasmon loss peak at 19.9 eV, and two decaying peaks at 40.2 and 61.4 eV. While the low-loss EELS of the nanoparticle after chemical reaction exhibits two major plasmon loss peaks at 14.9 and 19.1 eV, which agrees with that of Li_2S excellently[27].

The in situ TEM characterization indicates that the major reaction product after the chemical reaction between lithium and LGPS is Li_2S. The TEM results agree excellently with previous investigations[8, 10]. The products of $12Li_2S + 2Li_3P + Li_{3.75}Ge$ were reported previously after the reduction of LGPS against lithium[8, 10]. However, the formation of $Li_{3.75}Ge$ and Li_3P alloy, which is in accordance with theoretical calculations[30], was not proven unambiguously by in situ X-ray photoelectron spectroscopy[8]. Recent TEM results have also evidenced that Li_2S is the major reaction product[31].

Large volume expansion occurs during the electrochemical reaction between lithium and LGPS, which induces large stress, causing fracture of the LGPS particles. The fracture stress σ_c of a ceramic SE can be calculated using the following equation[32, 33]:

$$\sigma_c = K_{IC}(\pi d_c)^{-1/2}, \#(1)$$

where K_{IC} is the fracture toughness of the SE, and d_c is the critical flaw size such as the pore or grain size. As an example, let's calculate the fracture stress of LGPS SE. From Figure S11, the typical grain size is about 2.7 μm, and the fracture toughness K_{IC} of LGPS is about 0.34 MPa $m^{1/2}$ [33]. Plugging these values into Eqs. (1) yields σ_c of 116 MPa. Previous studies indicate that lithiation induced stress can reach GPa level[28, 29], which is sufficient to fracture SEs.

Based on the experimental SEM image, a schematic diagram of the Li_2S pulverization is presented in Figure 4a. The diagram consists of three layers of materials, namely, the pulverized Li_2S nano particles on the top (yellow), the non-pulverized Li_2S buffer layer (light pink) in the middle, and the LGPS rod at the bottom side (wathet). During lithiation, the thickness of the non-pulverized Li_2S buffer layer (h) keeps increasing and the stored elastic energy also increases. When the thickness of the buffer layer reaches a critical value, the stored elastic energy leads to pulverization of the whole buffer layer by releasing the elastic energy into surface energy and other forms of energy such as heat. To understand the pulverization process quantitatively, we consider a layer-by-layer pulverization of the LGPS rod, as shown in Figure 4b. Here we assume that all the pulverized Li_2S particles are in a cube shape and the edge length of the cubes is the same as the buffer layer thickness. The whole buffer layer is pulverized when its thickness reaches a critical value. During pulverization, some of the stored elastic energy are released as the surface energy of the pulverized Li_2S nano particles and others will be dissipated via wave propagation or heat etc. We further assume that the relationship between the released elastic energy and the surface energy is[34]:

$$U_e = \alpha E_s, \tag{2}$$

where U_e and E_s are the released elastic strain energy and surface energy of the pulverized Li_2S nano particles, respectively; $\alpha > 1$ was introduced to denote the contribution of wave propagation or other energy dissipation mechanism during the fragmentation process. The calculations of elastic strain energy and surface energy are presented in Supplementary Section 3.1. From Eqs.(2), the critical size of the new pulverized Li_2S particles is obtained as

$$h = \frac{\alpha D(5\gamma_{LS} + \gamma_{LGPS})}{u_e D + 4\alpha\gamma_{LS}}. \tag{3}$$

In Eqs. (3), the elastic strain energy per unit volume (μ_e) can be calculated by using finite element analysis (FEA) simulation. The cylindrical FEA models are presented in the inset of Figure 4d. We take the material properties of LGPS and Li_2S in literature[35, 36] for the FEA simulation. Using

the volume expansion of LGPS during lithiation as 50.0% (Figure S12), the calculated elastic strain energy (μ_e) as a function of the ratio of the Li_2S particle size (h) and diameter of the LGPS rod (D) is shown in Figure 4d, more detailed FEA simulations are shown in Supplementary Section 3.1.

By using the density functional theory (DFT) method (see Supplementary Section 4), the surface energies, γ_{LS} and γ_{LGPS}, were calculated as 13 and 3.8 eV/nm^2, respectively. The projected surface energy is also plotted in Figure 4d. Experimentally, the sizes of the Li_2S particles formed during pulverization of the LGPS particles of different sizes are shown in Figure 4c. To fit the experimentally measured particle size, $\alpha = 15$ was adopted and the critical size of the pulverized Li_2S particles (h) as a function of the diameter of the LGPS rod (D) is shown in Figure 4c as well. When the LGPS particle size is small (D < 10 μm), a strong size dependent pulverization behavior is clearly seen. The sizes of the Li_2S nanoparticles formed by pulverization of small LGPS particles are several times larger than those formed by pulverization of large LGPS particles.

Obviously, the size of the pulverized particle cannot be greater than the size of the LGPS particles, so the condition of $h = D$ determines the smallest LGPS that can be pulverized. As such, a LGPS paricle whose size is less than 0.87 μm cannot be pulverized (red star in Figure 4c). The size dependent behavior derived from modeling (black dashed lines) agrees well with the experimental observation (filled blue saquares, Figure 4c).

To predict the critical LGPS particle size more accurately, we constructed a spherical LGPS particle model to replace the infinite long LGPS rod model. The top/bottom hemispheres (Figure S13a) represent a Li_2S and a LGPS particle, respectively, and the stress distribution is shown in Figure S13b. The critical of LGPS particle size was estimated as (see details in Supplementary Section 3.2),

$$D = \frac{3\alpha(\gamma_{LGPS} + \gamma_{LS})}{2\mu_e}. \quad (4)$$

Using FEA simulation, the elastic strain energy per unit volume of the system is calculated to be 0.375 eV/nm^3 and the critical size D is estimated to be 1008 nm, which is very close to the experimental result, with a diameter of ~ 1.0 μm.

■ CONCLUSIONS

The chemomechanical failure of individual LGPS particles was investigated by in situ FIB-SEM. We revealed a strong size effect during the chemomechanical failure process of individual LGPS particles: when the particle size is greater than 3 μm, fracture and pulverization of the particles were always observed; when the particle size is less than 3 μm but larger than 1 μm, cracking of the particles took place; when the particle size is less than 1 μm, neither crack nor fracture of the particles was detected. This strong size effect is attributed to the energy balance between the elastic energy release caused by lithium reaction with LGPS and the surface energy release caused by fracture or pulverization of the particles. The size effect can be harnessed to alleviate the chemomechanical failure of LGPS, i.e. by tailoring the particle size of LGPS SE to less than 1 μm, the chemomechanical failure of LGPS SE may be mitigated.

■ ASSOCIATED CONTENT

Supporting Information

The Supporting Information is available free of charge on the ACS publications website.
Movie S1, in situ FIB/SEM movie showing the pulverization of a LGPS particle (30 μm). (AVI)
Movie S2, in situ FIB/SEM movie showing the pulverization of a LGPS particle (25 μm). (AVI)
Movie S3, in situ FIB/SEM movie showing the pulverization of a LGPS particle (3 μm). (AVI)
Movie S4, in situ FIB/SEM movie showing how lithium dendrites grew out of the cracks in LGPS. (AVI)
Movie S5, in situ FIB/SEM movie showing the pulverization of a LGPS particle (10 μm). (AVI)
Movie S6, in situ FIB/SEM movie showing the fracture of a LGPS particle (2.2 μm). (AVI)
Movie S7, in situ FIB/SEM movie showing the volume expansion of a LGPS particle (0.7 μm). (AVI)
Detailed descriptions of supporting movies and figures providing the strong size-dependent electro-chemo-mechanical fracture behavior of individual LGPS particles, supplementary methods and corresponding FEA modeling. (PDF)

■ AUTHOR INFORMATION

Corresponding Authors

E-mail: jyhuang8@hotmail.com; f.ding@unist.ac.kr; lqzhang@ysu.edu.cn; tangyongfu@ysu.edu.cn.

Author Contributions

L.Z., Y.T., F.D. and J.H. conceived and designed the project. J.Z., J.P.Z., X.L., Q.D., Z.W., J.C., P.J., Y.L. and Y.Y. fabricated the samples. J.Z., B.W. and J.Y. carried out the *in situ* experiments. L.Z., Y.T., F.D. and J.H. supervised the experiments. S.J.H., F.D. and J.H. co-wrote the paper. J.Z. and C.Z. contribute equally to this work. All the authors discussed the results and commented on the manuscript.

Notes

The authors declare no competing financial interest.

■ ACKNOWLEDGMENTS

This work was financially supported by the National Natural Science Foundation of China (Nos. 52022088, 51971245, 51772262, 21406191, U20A20336, 21935009), Beijing Natural Science Foundation (2202046), Fok Ying-Tong Education Foundation of China (No. 171064), Natural Science Foundation of Hebei Province (No. F2021203097, B2020203037, B2018203297), Hunan Innovation Team (2018RS3091), Institute for Basic Science (IBS-R019-D1) of South Korea. Part of this work was supported by the Assistant Secretary for Energy Efficiency and Renewable Energy, Vehicles Technology Office, of the U. S. Department of Energy under Contract No. DEAC02-05CH11231 (S. J. H).

■ REFERENCES

(1) Kamaya, N.; Homma, K.; Yamakawa, Y.; Hirayama, M.; Kanno, R.; Yonemura, M.; Kamiyama, T.; Kato, Y.; Hama, S.; Kawamoto, K.; Mitsui, A. A lithium superionic conductor. *Nat. Mater.* **2011,** *10*, 682-686.

(2) Wan, H.; Liu, S.; Deng, T.; Xu, J.; Zhang, J.; He, X.; Ji, X.; Yao, X.; Wang, C. Bifunctional Interphase-Enabled $Li_{10}GeP_2S_{12}$ Electrolytes for Lithium–Sulfur Battery. *ACS Energy Lett.* **2021,** *6*, 862-868.

(3) Li, X.; Ren, Z.; Norouzi Banis, M.; Deng, S.; Zhao, Y.; Sun, Q.; Wang, C.; Yang, X.; Li, W.; Liang, J.; Li, X.; Sun, Y.; Adair, K.; Li, R.; Hu, Y.; Sham, T.-K.; Huang, H.; Zhang, L.; Lu, S.; Luo, J.; Sun, X. Unravelling the Chemistry and Microstructure Evolution of a Cathodic Interface in Sulfide-Based All-Solid-State Li-Ion Batteries. *ACS Energy Lett.* **2019,** *4*, 2480-2488.

(4) Han, F.; Gao, T.; Zhu, Y.; Gaskell, K. J.; Wang, C. A Battery Made from a Single Material. *Adv. Mater.* **2015,** *27*, 3473-3483.

(5) Zhu, Y.; He, X.; Mo, Y. Origin of Outstanding Stability in the Lithium Solid Electrolyte Materials: Insights from Thermodynamic Analyses Based on First-Principles Calculations. *ACS Appl. Mater. Interfaces* **2015,** *7*, 23685-23693.

(6) Zhu, Y.; He, X.; Mo, Y. First principles study on electrochemical and chemical stability of solid electrolyte–electrode interfaces in all-solid-state Li-ion batteries. *J. Mater. Chem. A* **2016,** *4*, 3253-3266.

(7) Han, F.; Zhu, Y.; He, X.; Mo, Y.; Wang, C. Electrochemical Stability of $Li_{10}GeP_2S_{12}$ and $Li_7La_3Zr_2O_{12}$ Solid Electrolytes. *Adv. Energy Mater.* **2016,** *6*, 1501590.

(8) Wenzel, S.; Randau, S.; Leichtweiß, T.; Weber, D. A.; Sann, J.; Zeier, W. G.; Janek, J. Direct Observation of the Interfacial Instability of the Fast Ionic Conductor $Li_{10}GeP_2S_{12}$ at the Lithium Metal Anode. *Chem. Mater.* **2016,** *28*, 2400-2407.

(9) Madsen, K. E.; Bassett, K. L.; Ta, K.; Sforzo, B. A.; Matusik, K. E.; Kastengren, A. L.; Gewirth, A. A. Direct Observation of Interfacial Mechanical Failure in Thiophosphate Solid Electrolytes with Operando X-Ray Tomography. *Advanced Materials Interfaces* **2020,** *7*, 2000751.

(10) Tippens, J.; Miers, J. C.; Afshar, A.; Lewis, J. A.; Cortes, F. J. Q.; Qiao, H.; Marchese, T. S.; Di Leo, C. V.; Saldana, C.; McDowell, M. T. Visualizing Chemomechanical Degradation of a Solid-State Battery Electrolyte. *ACS Energy Lett.* **2019,** *4*, 1475-1483.

(11) Zhu, J.; Zhao, J.; Xiang, Y.; Lin, M.; Wang, H.; Zheng, B.; He, H.; Wu, Q.; Huang, J. Y.; Yang, Y. Chemomechanical Failure Mechanism Study in NASICON-Type $Li_{1.3}Al_{0.3}Ti_{1.7}(PO_4)_3$ Solid-State Lithium Batteries. *Chem. Mater.* **2020,** *32*, 4998-5008.

(12) Ye, L.; Li, X. A dynamic stability design strategy for lithium metal solid state batteries. *Nature* **2021,** *593*, 218-222.

(13) Porz, L.; Swamy, T.; Sheldon, B. W.; Rettenwander, D.; Frömling, T.; Thaman, H. L.; Berendts, S.; Uecker, R.; Carter, W. C.; Chiang, Y.-M. Mechanism of Lithium Metal Penetration through Inorganic Solid Electrolytes. *Adv. Energy Mater.* **2017,** *7*, 1701003.

(14) Cheng, E. J.; Sharafi, A.; Sakamoto, J. Intergranular Li metal propagation through polycrystalline $Li_{6.25}Al_{0.25}La_3Zr_2O_{12}$ ceramic electrolyte. *Electrochim. Acta* **2017,** *223*, 85-91.

(15) Han, F.; Westover, A. S.; Yue, J.; Fan, X.; Wang, F.; Chi, M.; Leonard, D. N.; Dudney, N. J.; Wang, H.; Wang, C. High electronic conductivity as the origin of lithium dendrite formation within solid electrolytes. *Nat. Energy* **2019,** *4*, 187-196.

(16) Shishvan, S. S.; Fleck, N. A.; McMeeking, R. M.; Deshpande, V. S. Growth rate of lithium filaments in ceramic electrolytes. *Acta Mater.* **2020,** *196*, 444-455.

(17) Qi, Y.; Ban, C.; Harris, S. J. A New General Paradigm for Understanding and Preventing Li Metal Penetration through Solid Electrolytes. *Joule* **2020,** *4*, 2599-2608.

(18) Kazyak, E.; Garcia-Mendez, R.; LePage, W. S.; Sharafi, A.; Davis, A. L.; Sanchez, A. J.; Chen, K.-H.; Haslam, C.; Sakamoto, J.; Dasgupta, N. P. Li Penetration in Ceramic Solid Electrolytes: Operando Microscopy Analysis of Morphology, Propagation, and Reversibility. *Matter* **2020,** *2*, 1025-1048.

(19) Ning, Z.; Jolly, D. S.; Li, G.; De Meyere, R.; Pu, S. D.; Chen, Y.; Kasemchainan, J.; Ihli, J.; Gong, C.; Liu, B.; Melvin, D. L. R.; Bonnin, A.; Magdysyuk, O.; Adamson, P.; Hartley, G. O.; Monroe, C. W.; Marrow, T. J.; Bruce, P. G. Visualizing plating-induced cracking in lithium-anode solid-electrolyte cells. *Nat. Mater.* **2021,** *20*, 1121-1129.

(20) Krauskopf, T.; Hartmann, H.; Zeier, W. G.; Janek, J. Toward a Fundamental Understanding of the Lithium Metal Anode in Solid-State Batteries—An Electrochemo-Mechanical Study on the Garnet-Type Solid Electrolyte $Li_{6.25}Al_{0.25}La_3Zr_2O_{12}$. *ACS Appl. Mater. Interfaces* **2019,** *11*, 14463-14477.

(21) Hao, S.; Daemi, S. R.; Heenan, T. M. M.; Du, W.; Tan, C.; Storm, M.; Rau, C.; Brett, D. J. L.; Shearing, P. R. Tracking lithium penetration in solid electrolytes in 3D by in-situ synchrotron X-ray computed tomography. *Nano Energy* **2021,** *82*, 105744.

(22) Chen, Y.; Wang, Z.; Li, X.; Yao, X.; Wang, C.; Li, Y.; Xue, W.; Yu, D.; Kim, S. Y.; Yang, F.; Kushima, A.; Zhang, G.; Huang, H.; Wu, N.; Mai, Y.-W.; Goodenough, J. B.; Li, J. Li metal deposition and stripping in a solid-state battery via Coble creep. *Nature* **2020,** *578*, 251-255.

(23) Xu, C.; Märker, K.; Lee, J.; Mahadevegowda, A.; Reeves, P. J.; Day, S. J.; Groh, M. F.; Emge, S. P.; Ducati, C.; Layla Mehdi, B.; Tang, C. C.; Grey, C. P. Bulk fatigue induced by surface reconstruction in layered Ni-rich cathodes for Li-ion batteries. *Nat. Mater.* **2021,** *20*, 84-92.

(24) Zhang, L.; Yang, T.; Du, C.; Liu, Q.; Tang, Y.; Zhao, J.; Wang, B.; Chen, T.; Sun, Y.; Jia, P.; Li, H.; Geng, L.; Chen, J.; Ye, H.; Wang, Z.; Li, Y.; Sun, H.; Li, X.; Dai, Q.; Tang, Y.; Peng, Q.; Shen, T.; Zhang, S.; Zhu, T.; Huang, J. Lithium whisker growth and stress generation in an in situ atomic force microscope–environmental transmission electron microscope set-up. *Nat. Nanotechnol.* **2020,** *15*, 94-98.

(25) Chen, J.; Zhao, C.; Xue, D.; Zhang, L.; Yang, T.; Du, C.; Zhang, X.; Fang, R.; Guo, B.; Ye, H.; Li, H.; Dai, Q.; Zhao, J.; Li, Y.; Harris, S. J.; Tang, Y.; Ding, F.; Zhang, S.; Huang, J. Lithium Deposition-Induced Fracture of Carbon Nanotubes and Its Implication to Solid-State Batteries. *Nano Letters* **2021,** *21*, 6859-6866.

(26) Liang, J.; Chen, N.; Li, X.; Li, X.; Adair, K. R.; Li, J.; Wang, C.; Yu, C.; Norouzi Banis, M.; Zhang, L.; Zhao, S.; Lu, S.; Huang, H.; Li, R.; Huang, Y.; Sun, X. $Li_{10}Ge(P_1–xSbx)2S_{12}$ Lithium-Ion Conductors with Enhanced Atmospheric Stability. *Chem. Mater.* **2020,** *32*, 2664-2672.

(27) Wang, Z.; Tang, Y.; Zhang, L.; Li, M.; Shan, Z.; Huang, J. In Situ TEM Observations of Discharging/Charging of Solid-State Lithium-Sulfur Batteries at High Temperatures. *Small* **2020,** *16*, 2001899.

(28) Liu, X. H.; Zhong, L.; Huang, S.; Mao, S. X.; Zhu, T.; Huang, J. Y. Size-Dependent Fracture of Silicon Nanoparticles During Lithiation. *ACS Nano* **2012,** *6*, 1522-1531.

(29) Huang, J. Y.; Zhong, L.; Wang, C. M.; Sullivan, J. P.; Xu, W.; Zhang, L. Q.; Mao, S. X.; Hudak, N. S.; Liu, X. H.; Subramanian, A.; Fan, H.; Qi, L.; Kushima, A.; Li, J. In Situ Observation of the Electrochemical Lithiation of a Single SnO_2 Nanowire Electrode. *Science* **2010,** *330*, 1515-1520.

(30) Ong, S. P.; Mo, Y.; Richards, W. D.; Miara, L.; Lee, H. S.; Ceder, G. Phase stability, electrochemical stability and ionic conductivity of the $Li_{10\pm1}MP_2X_{12}$ (M = Ge, Si, Sn, Al or P, and X = O, S or Se) family of superionic conductors. *Energy Environ. Sci.* **2013,** *6*, 148-156.

(31) Suyama, M.; Yubuchi, S.; Deguchi, M.; Sakuda, A.; Tatsumisago, M.; Hayashi, A. Importance of Li-Metal/Sulfide Electrolyte Interphase Ionic Conductivity in Suppressing Short-Circuiting of All-Solid-State Li-Metal Batteries. *J. Electrochem. Soc.* **2021,** *168*, 060542.

(32) Qu, M.; Woodford, W. H.; Maloney, J. M.; Carter, W. C.; Chiang, Y.-M.; Van Vliet, K. J. Nanomechanical Quantification of Elastic, Plastic, and Fracture Properties of $LiCoO_2$. *Adv. Energy Mater.* **2012,** *2*, 940-944.

(33) McGrogan, F. P.; Swamy, T.; Bishop, S. R.; Eggleton, E.; Porz, L.; Chen, X.; Chiang, Y.-M.; Van Vliet, K. J. Compliant Yet Brittle Mechanical Behavior of $Li_2S–P_2S_5$ Lithium-Ion-Conducting Solid Electrolyte. *Adv. Energy Mater.* **2017,** *7*, 1602011.

(34) Glenn, L. A.; Gommerstadt, B. Y.; Chudnovsky, A. A fracture mechanics model of fragmentation. *J. Appl. Phys.* **1986,** *60*, 1224-1226.

(35) Wang, Z. Q.; Wu, M.; Liu, G.; Lei, X.; Xu, B.; Ouyang, C. Elastic Properties of New Solid State Electrolyte Material $Li_{10}GeP_2S_{12}$: A Study from First-Principles Calculations. *International journal of electrochemical science* **2014,** *9*, 562-568.

(36) Khachai, H.; Khenata, R.; Bouhemadou, A.; Reshak, A. H.; Haddou, A.; Rabah, M.; Soudini, B. First principles study of the elastic properties in X_2S (X=Li, Na, K and Rb) compounds under pressure effect. *Solid State Commun.* **2008,** *147*, 178-182.

Figures

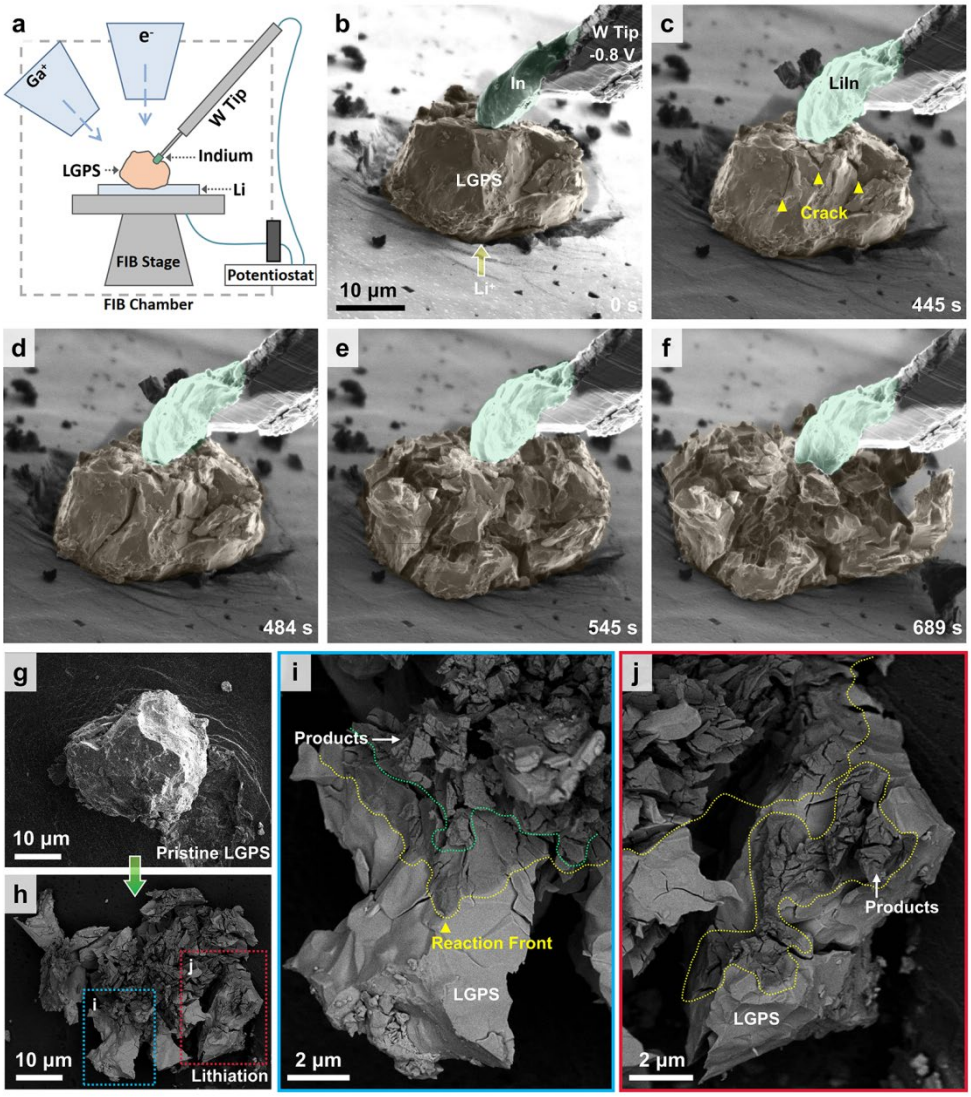

Figure 1. In situ observation of electrochemical reaction between lithium and individual LGPS particles. (a) Schematic of an electrochemical device comprising a Li anode, an LGPS SE, and a W tip coated with In as the counterelectrode inside a FIB-SEM. (b-f) Time lapse SEM images showing the lithiation process of a LGPS particle with a size of 30 μm. The formation of cracks (b-d) and pulverization (d-e) are evident. (g-j) Lithiation induced fracture and pulverization of LGPS particles. (g, h) Pulverization of an LGPS particle with a size of 30 μm. (i, j) Magnifications of the boxed regions in (h), showing the interfaces between the lithiated and non-lithiated particles (yellow dashed lines). Green dashed line in (i) marks the boundary between pulverization and non-pulverization.

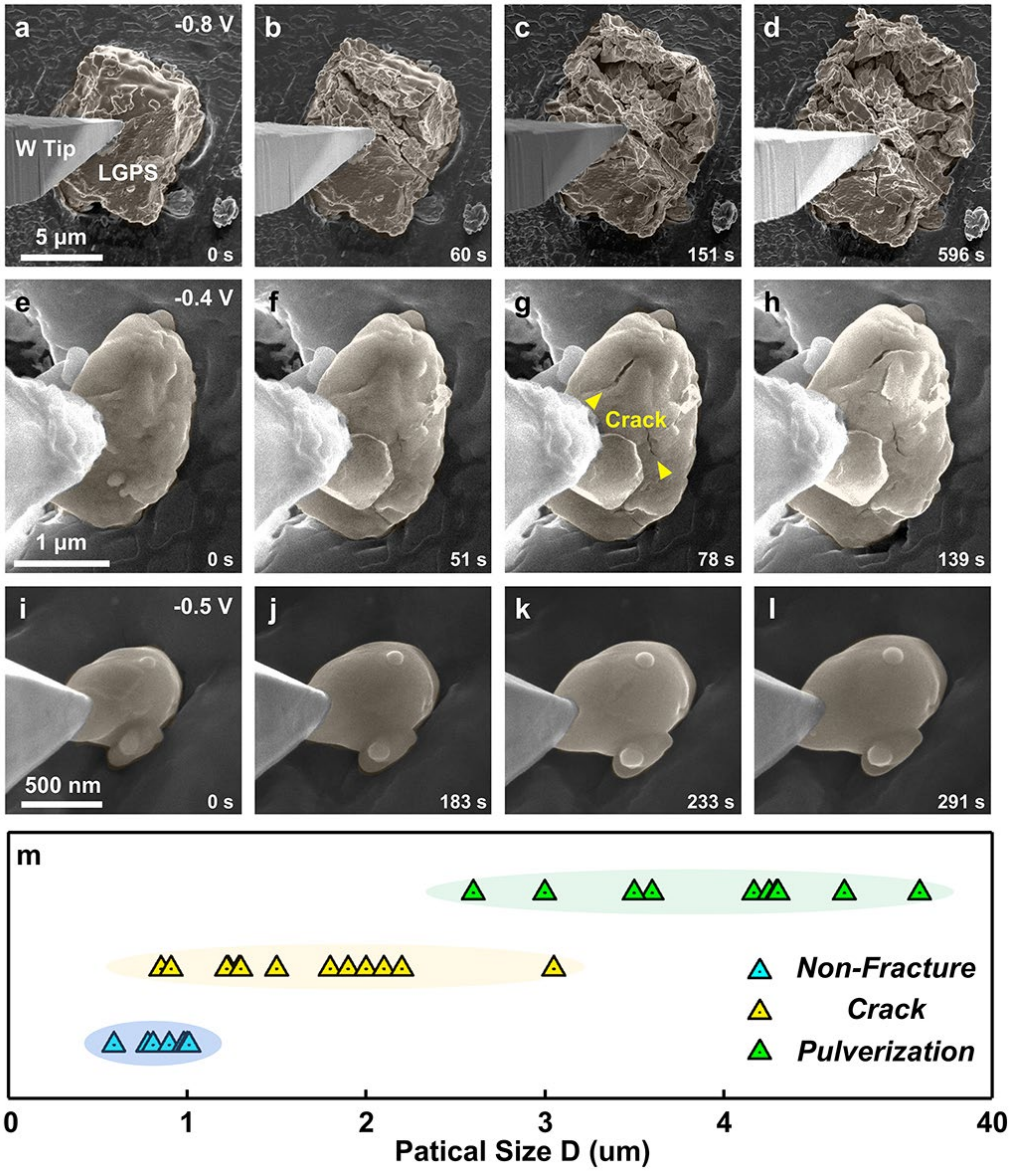

Figure 2. Size dependent fracture and pulverization of LGPS particles. The particle size in (a), (e) and (i) is 10, 2.2 and 0.7 μm, respectively. Fracture and pulverization occurred when the particle size is over 3 μm (a-d). Fracture but not pulverization took place when the particle size is between 3 μm and 1 μm (e-h). No fracture or pulverization took place when the particle size is less than 1 μm (i-l). (m) Statistic showing the size dependent electro-chemo-mechanical failure of LGPS particles. Three distinct size regimes were observed, namely, no fracture when $D < 1$ μm; fracture but not pulverization when 1 μm $< D <$ 3 μm; fracture and pulverization when $D >$ 3 μm.

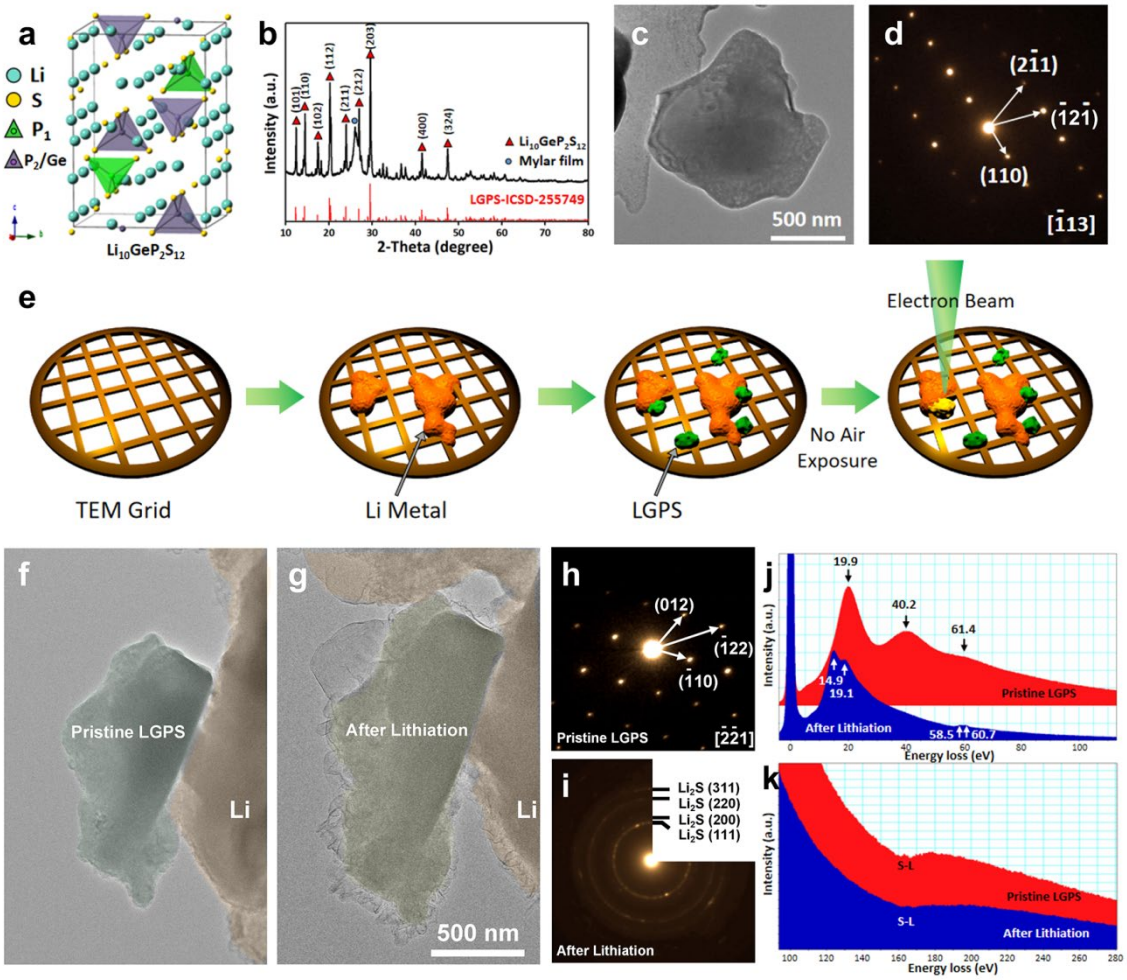

Figure 3. Characterization of the LGPS particles. (a) The structural model. The pristine LGPS has a tetragonal structure with $a = b = 8.71$ Å and $c = 12.61$ Å, and with a space group of $P4_2/nmc$. (b) X-ray diffraction pattern of the pristine LGPS powders. (c) A TEM bright filed image of a LGPS particle. (d) Electron diffraction pattern corresponding to (c), showing the [-113] zone axis of tetragonal LGPS. (e) Schematic of the in situ TEM experiments procedure. Lithium metal was scratched into a Cu grid. LGPS particles were drop casted onto the Cu grid with lithium metal. The electron beam was placed at the lithium metal where the LGPS particles were present nearby to initiate the chemical reaction between lithium and LGPS. The initial LGPS particle is single crystal (f, h). (f-i) In situ chemical lithiation of a LGPS particle. The starting particle (f) experienced significant volume expansion after lithiation (g). The pristine single crystal LGPS (h) turned into Li_2S (i) after lithiation. Low-loss (j) and core-loss (k) EELS of the pristine LGPS (red) and LGPS after lithiation (blue).

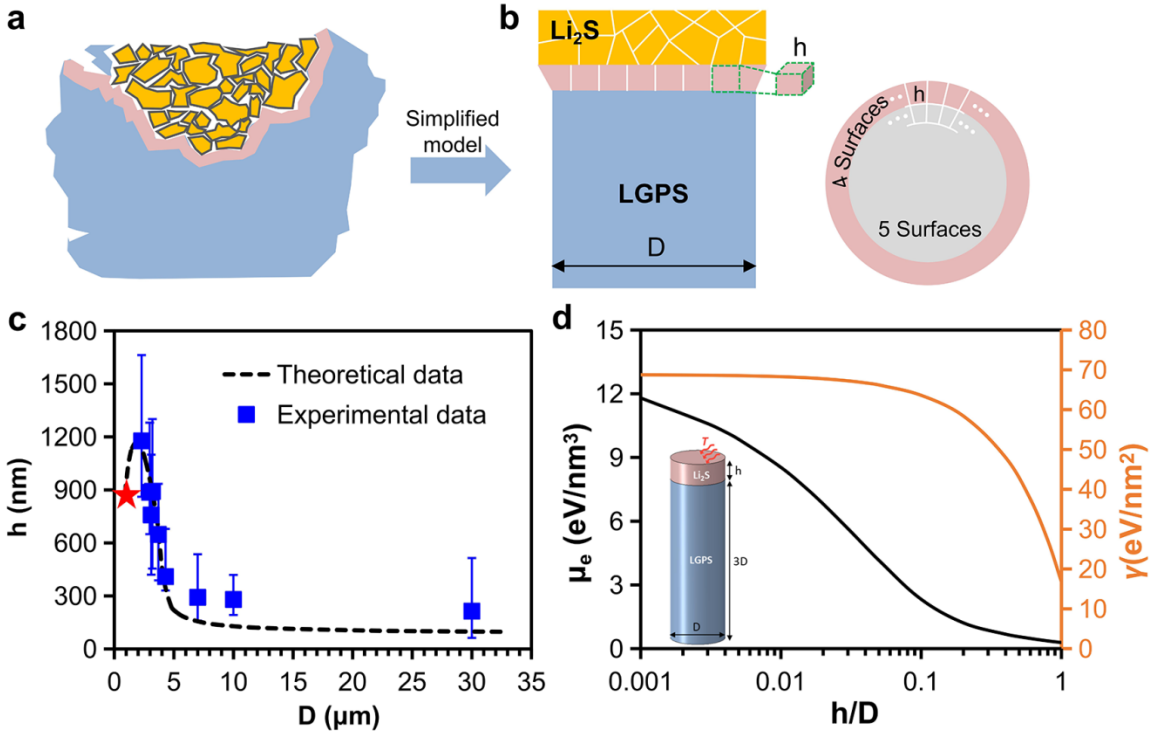

Figure 4. Theoretical modeling. (a) A schematic diagram showing the experimentally observed Li_2S pulverization process. (b) A simplified theoretical model of the pulverization of a LGPS rod. The right image is a top view of the theoretical model. (c) The calculated critical size of pulverized Li_2S particles (h) as a function of the diameter of the LGPS rod (D), comparing with experimental data. The red star marks the point of $h = D$. (d) The elastic strain energy (black line) and the projected surface energy (yellow line) as a functions of the ratio of the Li_2S particle size to the diameter of the LGPS rod.

Table of contents